

<b>Title</b>	Isolating the photovoltaic junction: atomic layer deposited TiO <sub>2</sub> -RuO <sub>2</sub> alloy Schottky contacts for silicon photoanodes
<b>Author(s)</b>	Hendricks, Olivia L.; Scheuermann, Andrew G.; Schmidt, Michael; Hurley, Paul K.; McIntyre, Paul C.; Chidsey, Christopher E. D.
<b>Publication date</b>	2016-08-22
<b>Original citation</b>	Hendricks, Olivia L.; Scheuermann, Andrew G.; Schmidt, Michael; Hurley, Paul K.; McIntyre, Paul C.; Chidsey, Christopher E. D. (2016) 'Isolating the Photovoltaic Junction: Atomic Layer Deposited TiO <sub>2</sub> -RuO <sub>2</sub> Alloy Schottky Contacts for Silicon Photoanodes'. ACS Applied Materials & Interfaces, 8 (36):23763-23773. doi: 10.1021/acsami.6b08558
<b>Type of publication</b>	Article (peer-reviewed)
<b>Link to publisher's version</b>	<a href="http://pubs.acs.org/doi/abs/10.1021/acsami.6b08558">http://pubs.acs.org/doi/abs/10.1021/acsami.6b08558</a> <a href="http://dx.doi.org/10.1021/acsami.6b08558">http://dx.doi.org/10.1021/acsami.6b08558</a> Access to the full text of the published version may require a subscription.
<b>Rights</b>	<b>Copyright © 2016 American Chemical Society. This document is the Accepted Manuscript version of a Published Work that appeared in final form in American Chemical Society Applied Materials &amp; Interfaces, copyright © American Chemical Society after peer review and technical editing by the publisher. To access the final edited and published work see <a href="http://pubs.acs.org/doi/abs/10.1021/acsami.6b08558">http://pubs.acs.org/doi/abs/10.1021/acsami.6b08558</a></b>
<b>Embargo information</b>	Access to this article is restricted until 12 months after publication by the request of the publisher.
<b>Embargo lift date</b>	2017-08-22
<b>Item downloaded from</b>	<a href="http://hdl.handle.net/10468/3260">http://hdl.handle.net/10468/3260</a>

Downloaded on 2018-08-23T18:39:41Z

## Isolating the photovoltaic junction: atomic layer deposited TiO-RuO alloy Schottky contacts for silicon photoanodes

Olivia L. Hendricks, Andrew G. Scheuermann, Michael Schmidt,  
Paul K. Hurley, Paul C McIntyre, and Christopher E. D. Chidsey

*ACS Appl. Mater. Interfaces*, **Just Accepted Manuscript** • DOI: 10.1021/acsami.6b08558 • Publication Date (Web): 22 Aug 2016

Downloaded from <http://pubs.acs.org> on August 29, 2016

### Just Accepted

“Just Accepted” manuscripts have been peer-reviewed and accepted for publication. They are posted online prior to technical editing, formatting for publication and author proofing. The American Chemical Society provides “Just Accepted” as a free service to the research community to expedite the dissemination of scientific material as soon as possible after acceptance. “Just Accepted” manuscripts appear in full in PDF format accompanied by an HTML abstract. “Just Accepted” manuscripts have been fully peer reviewed, but should not be considered the official version of record. They are accessible to all readers and citable by the Digital Object Identifier (DOI®). “Just Accepted” is an optional service offered to authors. Therefore, the “Just Accepted” Web site may not include all articles that will be published in the journal. After a manuscript is technically edited and formatted, it will be removed from the “Just Accepted” Web site and published as an ASAP article. Note that technical editing may introduce minor changes to the manuscript text and/or graphics which could affect content, and all legal disclaimers and ethical guidelines that apply to the journal pertain. ACS cannot be held responsible for errors or consequences arising from the use of information contained in these “Just Accepted” manuscripts.

1  
2  
3  
4  
5  
6  
7  
8  
9  
10  
11  
12  
13  
14  
15  
16  
17  
18  
19  
20  
21  
22  
23  
24  
25  
26  
27  
28  
29  
30  
31  
32  
33  
34  
35  
36  
37  
38  
39  
40  
41  
42  
43  
44  
45  
46  
47  
48  
49  
50  
51  
52  
53  
54  
55  
56  
57  
58  
59  
60

# Isolating the photovoltaic junction: atomic layer deposited TiO<sub>2</sub>-RuO<sub>2</sub> alloy Schottky contacts for silicon photoanodes

*Olivia L. Hendricks,<sup>†</sup> Andrew G. Scheuermann,<sup>‡</sup> Michael Schmidt,<sup>§</sup> Paul K. Hurley,<sup>§</sup> Paul C. McIntyre,<sup>\*‡</sup> Christopher E. D. Chidsey<sup>\*†</sup>*

<sup>†</sup> Department of Chemistry, Stanford University, Stanford, California 94305, United States

<sup>‡</sup> Department of Materials Science and Engineering, Stanford University, Stanford, California, 94305, United States

<sup>§</sup> Tyndall National Institute, University College Cork, Cork, Ireland

KEYWORDS: atomic layer deposition, Schottky junctions, MIS junctions, photoanodes, photovoltage, TiO<sub>2</sub> alloys

ABSTRACT: We have synthesized nanoscale TiO<sub>2</sub>-RuO<sub>2</sub> alloys by atomic layer deposition (ALD) that possess a high work function and are highly conductive. As such, they function as good Schottky contacts to extract photogenerated holes from n-type silicon while simultaneously interfacing with water oxidation catalysts. The ratio of TiO<sub>2</sub> to RuO<sub>2</sub> can be precisely controlled by the number of ALD cycles for each precursor. Increasing the composition above 16% Ru sets the electronic conductivity and the metal work function. No significant Ohmic loss for hole

1  
2  
3 transport is measured as film thickness increases from 3 to 45 nm for alloy compositions  $\geq 16\%$   
4 Ru. Silicon photoanodes with a 2 nm surface SiO<sub>2</sub> layer that are coated by these alloy Schottky  
5 contacts having compositions in the range of 13-46% RuO<sub>2</sub> exhibit average photovoltages of 525  
6 mV, with a maximum photovoltage of 570 mV achieved. Depositing TiO<sub>2</sub>-RuO<sub>2</sub> alloys on nSi  
7 sets a high effective work function for the Schottky junction with the semiconductor substrate,  
8 thus generating a large photovoltage that is isolated from the properties of an overlying oxygen  
9 evolution catalyst or protection layer.  
10  
11  
12  
13  
14  
15  
16  
17  
18  
19  
20  
21  
22  
23

24 1. INTRODUCTION: Metal-insulator-semiconductor (MIS) structures are promising candidates  
25 for integrated solar driven water splitting devices.<sup>1,2</sup> The photovoltage produced by an MIS  
26 junction depends on the strength of the built-in field, or Schottky barrier height. This built-in  
27 field, in turn, depends on the difference in work function between the semiconductor and the  
28 metal, taking charges and interface fields into account.<sup>3</sup> In the 1970s, Green and co-workers  
29 found that a conductor with a sufficiently high work function produced a surface inversion layer  
30 at the semiconductor/insulator interface that helped screen interface traps and promote minority  
31 carrier transport across the insulator. As long as the insulator was kept sufficiently thin (1-3 nm),  
32 it could simultaneously enable interface defect passivation and facile charge transport by  
33 tunneling.<sup>3-6</sup> In recent examples of this approach for water oxidation, the metal layer has both set  
34 the built-in field to extract photogenerated carriers from the semiconductor and also functioned  
35 as the catalyst for water oxidation.  
36  
37  
38  
39  
40  
41  
42  
43  
44  
45  
46  
47  
48  
49  
50  
51  
52  
53  
54

55 Recent advances in atomic layer deposition (ALD) of metal oxide protection layers have made it  
56 possible to suppress oxidative corrosion of semiconductor materials, such as silicon, that would  
57  
58  
59  
60

1  
2  
3 otherwise be unstable under the conditions required for water oxidation.<sup>1,2,7-13</sup> Incorporation of  
4 such protection layers into the MIS junction, however, has compromised the photovoltages  
5 commonly reported for these devices. An ideal MIS junction using silicon has a theoretical  
6 maximum open circuit voltage of 700-800 mV.<sup>14</sup> Previous reports of silicon MIS photoanodes,  
7 however, have fallen well below this benchmark. For example, nSi photoanodes protected by  
8 highly conductive TiO<sub>2</sub> have reported photovoltages of ~400 mV,<sup>2</sup> with some devices only  
9 achieving 200-250 mV.<sup>13</sup>  
10  
11  
12  
13  
14  
15  
16  
17  
18  
19

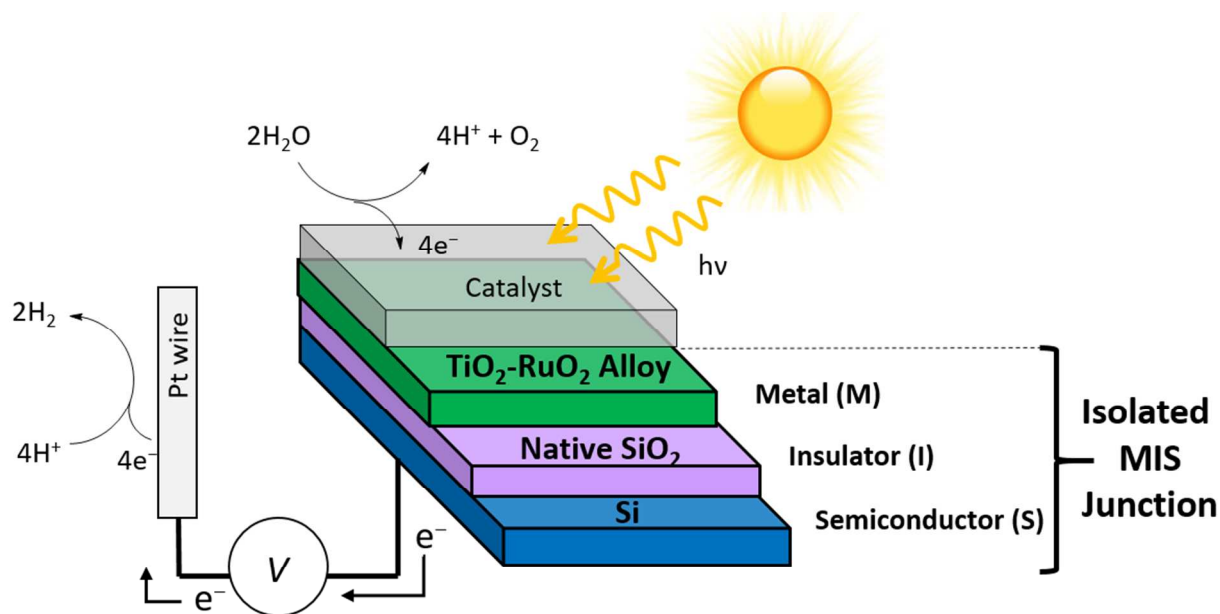
20  
21  
22 Although TiO<sub>2</sub> is highly stable under the conditions required for water oxidation,<sup>15</sup> its electrical  
23 properties are difficult to control and are not ideal for simultaneously generating the maximum  
24 photovoltage at high photocurrent.<sup>12</sup> The conductivity of TiO<sub>2</sub> films reported by different  
25 research groups has been inconsistent, even in cases where the same precursor species and  
26 similar temperatures and pressures are used in ALD film deposition.<sup>2,11</sup> Evidently, the factors  
27 controlling TiO<sub>2</sub> conductivity in ultrathin and amorphous or weakly-crystalline ALD-grown  
28 films are not easily controlled. Moreover, the TiO<sub>2</sub> causes photovoltage losses regardless of its  
29 hole-conducting capabilities.<sup>12</sup> If the TiO<sub>2</sub> is highly conductive, it should set the built-in field in  
30 the semiconductor. Highly-conductive n-type TiO<sub>2</sub> is expected to have a work function near its  
31 conduction band edge, leading to a small built-in field with nSi. Conversely, if the TiO<sub>2</sub> behaves  
32 as an insulator, increasing its thickness leads to photovoltage losses from a charge extraction  
33 barrier at the semiconductor/insulator interface.<sup>12</sup>  
34  
35  
36  
37  
38  
39  
40  
41  
42  
43  
44  
45  
46  
47  
48  
49  
50

51  
52  
53 We have optimized the electrical properties of TiO<sub>2</sub> by alloying it with RuO<sub>2</sub> in an all-ALD  
54 process to make a highly conductive, high work function Schottky contact to n-type silicon. Our  
55  
56  
57  
58  
59  
60

1  
2  
3 work was motivated by the success of the dimensionally stable anode (DSA) for industrial  
4 chlorine evolution, which occurs at similarly positive potentials to water oxidation.<sup>16-18</sup> Today's  
5 DSAs consist of a thick (a few microns), mixed TiO<sub>2</sub>/RuO<sub>x</sub> coating prepared by thermal  
6 decomposition of appropriate precursors at high temperature. The resulting electrode is known  
7 for its high conductivity and durability.<sup>16-18</sup> We sought to create an ultra-thin analogue to the  
8 DSA and to understand the chemical and electrical properties of similar TiO<sub>2</sub>-RuO<sub>2</sub> alloys  
9 prepared by ALD.  
10  
11  
12  
13  
14  
15  
16  
17  
18  
19  
20  
21

22 As illustrated in Figure 1, the TiO<sub>2</sub>-RuO<sub>2</sub> alloy/SiO<sub>2</sub>/n-type silicon junction functions as an  
23 isolated MIS photoanode. Isolating the photovoltaic junction from the electronic characteristics  
24 of the catalyst or from overlying protection layers allows for optimization of the latter  
25 components for catalytic efficiency and stability without compromising the photovoltage or  
26 photocurrent of the MIS junction. Alloyed TiO<sub>2</sub>-RuO<sub>2</sub> films are efficient hole conducting  
27 contacts to silicon and possess a high work function of 5-5.2 eV. Alloys ranging from 13-46%  
28 Ru showed an average photovoltage of 525 mV, with a maximum observed photovoltage of 570  
29 mV. This is a significant improvement over previously reported electrodes with similarly  
30 conductive but non-alloyed TiO<sub>2</sub>. Hole conduction through the films shows no significant Ohmic  
31 loss as film thickness is increased from 3 to 45 nm. Thus, nanoscale RuO<sub>2</sub>-TiO<sub>2</sub> alloys provide  
32 Schottky junction photoanodes with both high conductance and high photovoltage, independent  
33 of film thickness. Most importantly, the built-in-field is set by the TiO<sub>2</sub>-RuO<sub>2</sub> alloy, not by the  
34 overlying catalyst.  
35  
36  
37  
38  
39  
40  
41  
42  
43  
44  
45  
46  
47  
48  
49  
50  
51  
52  
53  
54  
55  
56  
57  
58  
59  
60

1  
2  
3 This work illustrates the significant opportunity presented by alloyed and structured ALD metal  
4 oxide films to control and isolate the properties of Schottky contacts to semiconductors. Alloying  
5  
6 oxide films to control and isolate the properties of Schottky contacts to semiconductors. Alloying  
7  
8 by ALD enables the flexibility to incorporate a wide variety of materials that could, in principle,  
9  
10 be optimized for any semiconductor absorber. This is particularly significant for semiconductors  
11  
12 that cannot be doped to form high-quality homojunctions. Previous work has demonstrated that  
13  
14 ALD  $\text{CoO}_x$  can be used to make a good Schottky contact to n-type silicon, and photovoltages  
15  
16 greater than 500 mV were observed.<sup>10</sup> Similarly high photovoltages, however, were not observed  
17  
18 when ALD  $\text{NiO}_x$  and  $\text{FeO}_x$  were used instead, despite similar reported work functions among  
19  
20 these materials.<sup>19,20</sup> These inconsistencies suggest that further study is needed to understand the  
21  
22 requirements for these types of Schottky contacts. Here, we present a rigorous characterization of  
23  
24  $\text{TiO}_2$ - $\text{RuO}_2$  alloys as model Schottky contacts to n-type silicon.  
25  
26



52  
53  
54  
55  
56  
57  
58  
59  
60

**Figure 1.** Schematic of the silicon photoanodes fabricated in this study using an isolated MIS junction. The  $\text{TiO}_2$ - $\text{RuO}_2$  alloy is sufficiently conductive to function as the metal. The native  $\text{SiO}_2$ , which is approximately 1.5-2 nm in thickness, is the insulator.

## 2. RESULTS AND DISCUSSION:

### 2.1 CHARACTERIZATION OF TiO<sub>2</sub>-RuO<sub>x</sub> ALLOY FILMS

TiO<sub>2</sub> films were grown using half-cycle dosing of tetrakis-(dimethylamido)titanium (TDMAT) and water vapor.<sup>21</sup> RuO<sub>x</sub> films were grown using bis(2,4-dimethylpentadienyl) ruthenium (Ru(DMPD)<sub>2</sub>) and oxygen.<sup>22,23</sup> ALD of ruthenium is known to produce a range of oxidation states.<sup>22-28</sup> For now, we will refer to the oxidation state of ruthenium in our ALD films as RuO<sub>x</sub> to preserve generality. TiO<sub>2</sub>-RuO<sub>x</sub> alloyed films were grown by an ALD alloying process in which individual cycles of TiO<sub>2</sub> and Ru were alternated. The ratio of TiO<sub>2</sub> to RuO<sub>x</sub> cycles was chosen to control the Ru content in the film, and this cycle ratio was repeated for a designated number of ALD super-cycles. For example, one super-cycle of a 1:4 alloy would include one ALD cycle of TiO<sub>2</sub> followed by four ALD cycles of RuO<sub>x</sub>. This process was repeated for multiple super-cycles to vary the film thickness.

**Figure 2** shows atomic layer deposition data for **(A)** TiO<sub>2</sub>, **(B)** RuO<sub>x</sub>, and **(C)** TiO<sub>2</sub>-RuO<sub>x</sub> alloyed films. The TiO<sub>2</sub> film thickness was measured by ellipsometry. As seen in **Figure 2A**, TiO<sub>2</sub> film thickness increases linearly with the number of ALD cycles, and the growth per cycle is calculated to be ~0.5 Å/cycle. Ru film thickness was calculated using X-ray photoelectron spectroscopy (XPS) based on the silicon peak attenuation by the ruthenium overlayer. The details of these calculations are described in the Supporting Information. As seen in **Figure 2B**, Ru film thickness increases linearly with the number of ALD cycles. The growth per cycle is 0.5 Å/cycle, which is higher than previously reported for ruthenium ALD.<sup>22-28</sup> There is an initiation delay of approximately 10 cycles before steady-state ALD of Ru is achieved. This delay is quite low compared to typical noble metal ALD, which often exhibits > 50-100 cycles of initiation delay.



TiO<sub>2</sub>-RuO<sub>x</sub> alloyed film thicknesses were calculated using X-ray reflectivity (XRR), and the thickness of select samples was confirmed by transmission electron microscopy (TEM) (**Figure S5**). **Figure 2C** shows the % Ru incorporation relative to Ti calculated from XPS for alloyed films fabricated for several different TiO<sub>2</sub>-RuO<sub>x</sub> ALD cycle ratios. As expected, the % Ru content increases as the relative number of Ru cycles increases. An 8:1 TiO<sub>2</sub> to RuO<sub>x</sub> cycle ratio results in 13% Ru, while a 1:4 TiO<sub>2</sub> to Ru cycle ratio yields 46% Ru. The % Ru content is highly reproducible, as well. Thus, the ALD alloying process can produce films over a wide composition range with very precise control over the Ru composition.

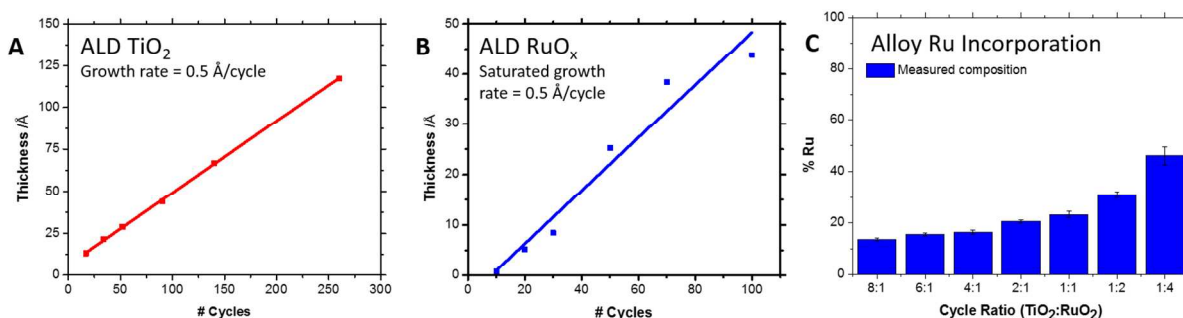


**Figure 2.** (A) Film thickness as a function of the number of ALD cycles for the TiO<sub>2</sub> ALD process (B) Film thickness as a function of the number of ALD cycles for the RuO<sub>x</sub> ALD process. (C) The fraction of Ru incorporation into the TiO<sub>2</sub>-RuO<sub>x</sub> alloyed films as a function of ALD cycle ratio. The % Ru was calculated taking only Ru and Ti into consideration, ie % Ru = Ru / (Ru + Ti). Error bars reflect the standard deviation in % Ru. Film thickness for pure TiO<sub>2</sub> films was measured using ellipsometry. Film thickness for RuO<sub>x</sub> films was determined by XPS.

**Figure 3** shows high resolution XPS spectra for (A) a 5 nm TiO<sub>2</sub> film and (B) and a 4 nm Ru film. Details of the peak assignments and peak fitting procedures are described in the Supporting Information. Thin ALD films were chosen for analysis so that the substrate Si peaks were

1  
2  
3 detectable. All peak positions are referenced to the Si 2p peak at 99 eV. **Table 1** summarizes the  
4  
5  
6 calculated atomic compositions.

7  
8 The Ti 2p spectrum in **Figure 3A** shows two peaks at 458.9 eV and 464.7 eV corresponding to  
9  
10 the Ti 2p<sub>3/2</sub> and Ti 2p<sub>1/2</sub> peaks, respectively. The O1s peak shows three major components. The  
11  
12 lowest binding energy component at 530.3 eV corresponds to oxygen in TiO<sub>2</sub>,<sup>29</sup> while the highest  
13  
14 binding energy component at 532.0 eV corresponds to oxygen in SiO<sub>2</sub>.<sup>30</sup> The component at 531.2  
15  
16 eV is associated with carbon-bound oxygen. Based on the integrated areas under the Ti 2p peak  
17  
18 and the O 1s component at 530.3 eV, the ratio of Ti to O was calculated to be 1:2, or fully  
19  
20 oxidized TiO<sub>2</sub>. No evidence of other Ti oxidation states were observed, particularly Ti,<sup>3+</sup> which  
21  
22  
23  
24  
25  
26  
27  
28  
29  
30  
31  
32  
33  
34  
35  
36  
37  
38  
39  
40  
41  
42  
43  
44  
45  
46  
47  
48  
49  
50  
51  
52  
53  
54  
55  
56  
57  
58  
59  
60 would appear as a shoulder at lower binding energy in the Ti 2p spectrum.

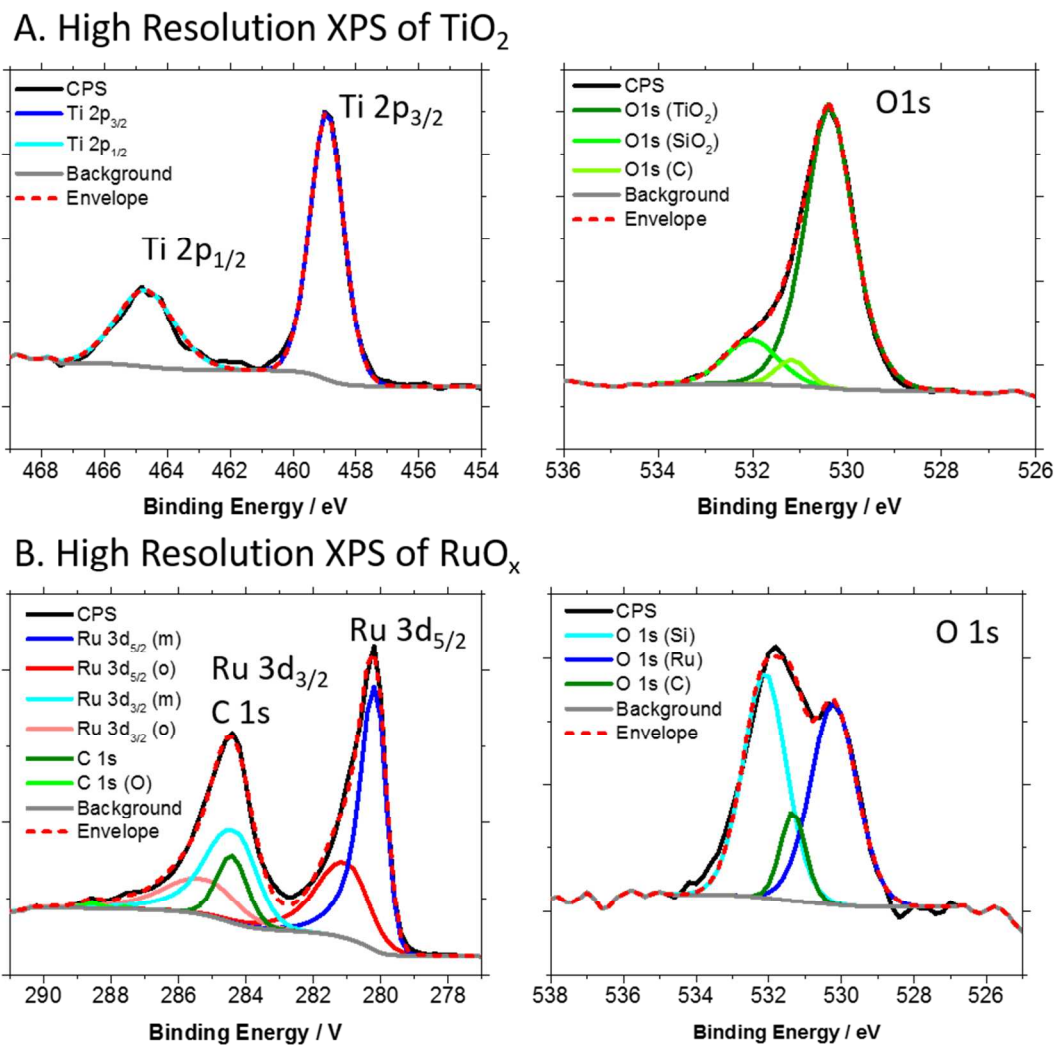


**Figure 3.** High resolution XPS spectra for (A) a 5 nm TiO<sub>2</sub> film on Si and (B) a 4 nm RuO<sub>x</sub> film on Si. Lower binding energy peaks associated with metallic Ru are denoted (m) and typically have a smaller full width at half max. Higher binding energy peaks associated with oxidized Ru are denoted (o) and typically have a larger full width at half max. The specific binding energy of the oxide peaks suggests hydrated RuO<sub>2</sub>.

The RuO<sub>x</sub> 3d spectrum in **Figure 3B** was fit with six components: two Ru 3d<sub>5/2</sub> peaks and their associated 3d<sub>3/2</sub> peaks, adventitious C 1s at 284.4 eV, and higher binding energy C 1s peaks for

1  
2  
3 carbon-oxygen species. The lower binding energy Ru 3d<sub>5/2</sub> peak at 280.1 eV corresponds to  
4  
5 metallic Ru, while the higher binding energy Ru 3d<sub>5/2</sub> peak at 281.0 eV corresponds to RuO<sub>2</sub>.<sup>31,32</sup>  
6  
7 The binding energy of the RuO<sub>2</sub> peak suggests that the oxide is hydrated. Hydrated RuO<sub>2</sub>  
8  
9 typically appears at higher binding energy, ≥ 280.8 eV, whereas anhydrous RuO<sub>2</sub> appears closer  
10  
11 to 280.6 eV.<sup>31</sup> RuO<sub>2</sub> is known to have a high affinity for water, even under ultra-high vacuum  
12  
13 conditions.<sup>33,34</sup>  
14  
15  
16  
17  
18  
19

20 The O1s spectrum was fit with three components. Peaks at 532.0 eV and 531.1 eV are associated  
21  
22 with SiO<sub>2</sub> and carbon-bound oxygen, respectively. These peaks appear at the same binding  
23  
24 energy as in the O 1s spectrum for TiO<sub>2</sub>. The lowest binding energy peak at 530.2 eV  
25  
26 corresponds to oxygen in RuO<sub>2</sub>. Its binding energy also suggests hydrated RuO<sub>2</sub>, as the O1s peak  
27  
28 for anhydrous RuO<sub>2</sub> typically appears at 529.4 eV.<sup>31,32</sup>  
29  
30  
31  
32  
33

34 **Table 1.** Atomic % calculated from integrated areas of high resolution XPS spectra, scaled  
35  
36 according to the appropriate relative sensitivity factors (RSF).  
37  
38  
39  
40  
41

Atom	Atom % in ALD TiO <sub>2</sub>	Atom % in ALD RuO <sub>x</sub>	Atomic % in 33% Ru ALD alloy
Ru (metallic)	-	13.4	-
Ru (oxide)	-	7.3	5.8
Ti	22.1	-	11.4
C	19.6	32.0	29.2
O (Si)	7.4	14.0	9.2
O (Ru)	-	13.4	12.5

O (C)	1.2	3.2	1.6
O (Ti)	44.3	-	22.5
Si (metal)	1.7	8.9	3.2
Si (SiO <sub>2</sub> )	3.7	6.9	4.6

Depth profiling analysis indicates that RuO<sub>2</sub> is only present at the surface of the ALD-Ru film (**Figure S8**). It is worth noting that ALD of Ru commonly results in a metallic film, with highly oxidizing conditions (high P<sub>O<sub>2</sub></sub>, long O<sub>2</sub> exposure time, O<sub>2</sub> plasma, ozone, etc.) required to deposit RuO<sub>2</sub>.<sup>22–28</sup> This is typically attributed to the slow kinetics of oxygen diffusion through Ru films, and the requirement that a subsurface oxygen layer form during the ALD process to generate RuO<sub>2</sub>.<sup>22,35,36</sup> Attempts to deposit RuO<sub>2</sub> directly in our ALD reactor using higher partial pressures of O<sub>2</sub> have so far been unsuccessful.

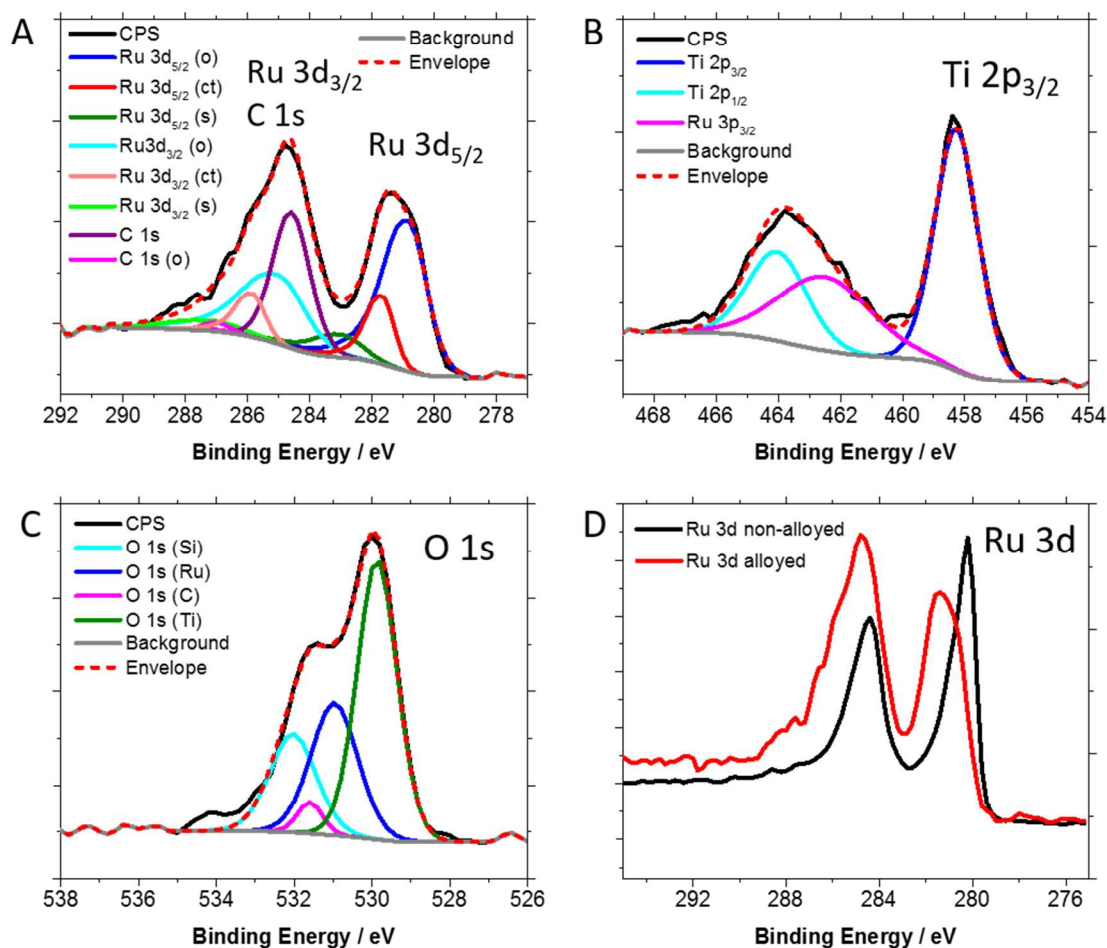


**Figure 4.** Representative high resolution XPS spectra for 6 nm 33% RuO<sub>x</sub> alloy. **(A)** Ru 3d peak and its various components. Peaks associated with oxidized Ru are denoted (o), peaks associated with a potential charge transfer between Ru and Ti are denoted (ct), and satellite peaks are denoted (s). **(B)** Ti 2p peak and its various components, including the overlapping Ru 3p<sub>3/2</sub> peak **(C)** O 1s peak and its various components **(D)** Comparison of the Ru 3d spectra in a 6 nm 33% RuO<sub>x</sub> alloy film vs a 4 nm RuO<sub>x</sub> film.

**Figure 4** shows representative XPS spectra for a 6 nm 33% Ru alloy film. As shown in **Figure 4A**, the Ru 3d spectrum was fit with three Ru 3d<sub>5/2</sub> peaks, their associated Ru 3d<sub>3/2</sub> peaks and the

1  
2  
3 same series of C 1s peaks. In this case, however, the lowest energy Ru 3d<sub>5/2</sub> peak at 280.8 eV  
4  
5 corresponds to oxidized RuO<sub>2</sub> instead of metallic Ru.<sup>31,32</sup> The highest binding energy Ru 3d<sub>5/2</sub>  
6  
7 peak at 283 eV and its corresponding Ru 3d<sub>3/2</sub> peak are most likely satellite peaks, commonly  
8  
9 observed in RuO<sub>2</sub> spectra due to core-hole screening.<sup>33</sup> There are two possible justifications for  
10  
11 the middle Ru 3d<sub>5/2</sub> component at 281.6 eV. One possibility is that this component represents  
12  
13 hydrated RuO<sub>2</sub>. Alternatively, this component could indicate a partial shift of the Ru 3d<sub>5/2</sub> peak  
14  
15 to higher binding energy. Previous literature reports have suggested that such a shift reflects  
16  
17 charge transfer from Ru to Ti.<sup>37</sup> In this case, the Ru 3d shift to higher binding energy would be  
18  
19 accompanied by a shift to lower binding energy in the Ti 2p spectrum. In fact, the Ti 2p<sub>3/2</sub> peak  
20  
21 in the 33% Ru alloy indeed shifts to lower binding energy, appearing at 458.3 eV instead of the  
22  
23 458.9 eV measured for non-alloyed TiO<sub>2</sub>. Thus, it seems likely that charge transfer between Ru  
24  
25 and Ti is occurring, supporting a solid solution model for TiO<sub>2</sub>-RuO<sub>2</sub> alloys.  
26  
27  
28  
29  
30  
31  
32  
33

34 **Table 1** lists the calculated atomic % for the components of the 33% Ru alloy film. The oxide  
35  
36 stoichiometries are calculated to be RuO<sub>2.1</sub> and TiO<sub>1.9</sub>. Thus, both Ti and Ru appear to be fully  
37  
38 oxidized. Comparing the Ru 3d spectrum in the alloyed samples to the non-alloyed ruthenium  
39  
40 samples also suggests a different oxidation state of ruthenium in the alloyed samples, as shown  
41  
42 in **Figure 4D**. The Ru 3d peaks are broader and have shifted to higher binding energy by 1 eV  
43  
44 compared to the ALD-Ru film, signifying a more oxidized chemical state.<sup>22,31,32,37</sup> Under ALD  
45  
46 conditions, the presence of TiO<sub>2</sub> appears to favor the deposition of RuO<sub>2</sub> over metallic Ru.  
47  
48  
49  
50  
51  
52

53 To further investigate the distribution of Ru ions in the TiO<sub>2</sub> matrix, scanning Auger electron  
54  
55 spectroscopy (AES) was performed to generate 2D elemental maps for a 15 nm 16% Ru alloy  
56  
57  
58  
59  
60

1  
2  
3 and a 60 nm 46% Ru alloy (**Figure S9**). There appears to be no long-range phase separation  
4  
5 between the TiO<sub>2</sub> and RuO<sub>2</sub> in these films. At the beam resolution limit of approximately 25 nm,  
6  
7 no discrete areas of TiO<sub>2</sub> or RuO<sub>2</sub> are observed.  
8  
9

10  
11  
12 The structure of these films was also characterized by grazing incidence X-ray diffraction  
13 (GIXRD). GIXRD patterns from a series of films ranging in composition from 0-46% Ru show  
14  
15 no individual rutile or anatase phase reflections (**Figure S10**). Overall, the absence of discernible  
16  
17 reflections from the TiO<sub>2</sub>-RuO<sub>2</sub> films suggests that the ALD-grown alloys lack long-range  
18  
19 crystalline order.  
20  
21  
22  
23

24  
25  
26  
27 Finally, the optical properties of these films were characterized by ultraviolet-visible (UV-vis)  
28  
29 spectroscopy. Absorbance spectra from 200-1800 nm were collected for 10 nm alloy films  
30  
31 ranging from 13-46% Ru grown on fused quartz substrates (**Figure S11**). Increased absorbance  
32  
33 in the visible region is observed for higher % Ru alloys. A similar effect is observed for nitrogen  
34  
35 doping of TiO<sub>2</sub> films,<sup>38,39</sup> providing additional evidence that RuO<sub>2</sub> is incorporated into the TiO<sub>2</sub>  
36  
37 lattice uniformly, as opposed to in discrete islands. Nevertheless, absorbance losses for 10 nm  
38  
39 films were minimal. At 550 nm, 90% of the light is still transmitted for a 21% TiO<sub>2</sub>-RuO<sub>2</sub> alloy,  
40  
41 which showed the highest absorption among all the alloy compositions at this wavelength.  
42  
43  
44  
45  
46  
47

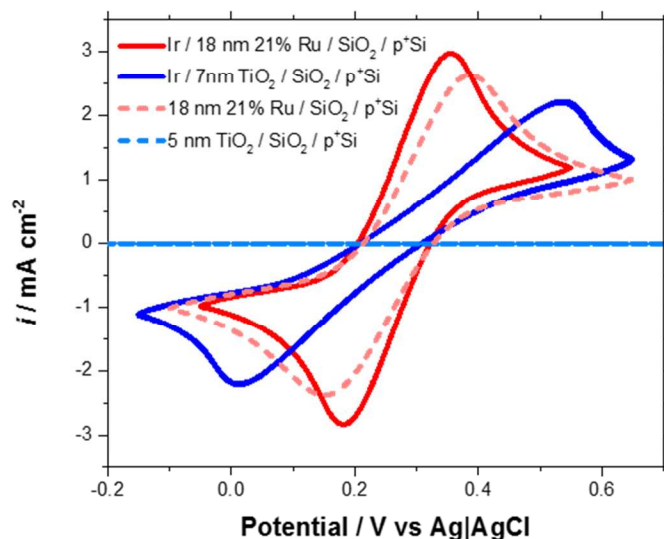
## 48 2.2 CONDUCTIVITY OF TiO<sub>2</sub>-RuO<sub>2</sub> ALLOY FILMS

49  
50

51  
52 In order for TiO<sub>2</sub>-RuO<sub>2</sub> alloys to set the built-in field, they must be sufficiently conductive to  
53  
54 induce the necessary band banding in the semiconductor. TiO<sub>2</sub>-RuO<sub>2</sub> conductivity is assessed by  
55  
56 measuring the half peak-to-peak (HP2P) splitting of the ferri/ferrocyanide (FFC) redox couple  
57  
58  
59  
60



1  
2  
3 using cyclic voltammetry,  $E_{\text{HP2P}} = E_{\text{peak}} - E_{1/2}$  where  $E_{1/2}$  is the average of the cathodic and  
4 anodic peak potentials  $[(E_{\text{pa}} + E_{\text{pc}})/2]$ . A lower half peak-to-peak splitting indicates higher  
5 conductivity of the ALD alloy layer. **Figure 5** compares the HP2P splitting in FFC of  $\text{TiO}_2$ - $\text{RuO}_2$   
6 alloy films and non-alloyed  $\text{TiO}_2$  films with and without an iridium coating. When iridium is  
7 used, the HP2P splitting of an 18 nm 21% Ru alloy (solid red) is already more conductive than a  
8 7 nm  $\text{TiO}_2$  film (solid blue). More significantly, the alloy films can function as metallic  
9 electrodes themselves, without an iridium layer. An 18 nm 21% Ru alloy (dashed red) has a  
10 HP2P of 117 mV, which is only slightly higher than the lowest HP2P values of 70-80 mV  
11 typically observed for Ir / 2 nm  $\text{SiO}_2$  /  $\text{p}^+\text{Si}$  anodes.  $\text{TiO}_2$  alone is unable to mediate electron  
12 transfer in FFC,<sup>1</sup> as indicated by the horizontal dashed blue line in **Figure 5**.



48 **Figure 5.** Half peak-to-peak (HP2P) splitting in 10 mM ferri/ferrocyanide, 1 M KCl of ALD  
49 films with (solid) and without (dashed) an iridium contact layer. The  $\text{TiO}_2$ - $\text{RuO}_2$  alloy films (red)  
50 are significantly more conductive than  $\text{TiO}_2$  alone (blue), as evidenced by the smaller HP2P.  
51 Moreover,  $\text{TiO}_2$  without iridium exhibits no electrochemical response.  
52  
53  
54  
55  
56  
57  
58  
59  
60

1  
2  
3 In fact, the HP2P splitting shows very little dependence on thickness for a wide range of alloy  
4 compositions. **Figure 6A** shows the HP2P splitting as a function of TiO<sub>2</sub>-RuO<sub>2</sub> alloy film  
5 thickness for compositions ranging from 16-46% RuO<sub>2</sub> on p<sup>+</sup>Si. Film thickness was varied from  
6 3-45 nm. Although thin compared to the dimensionally stable anode (DSA), this range  
7 encompasses the extremes of typical ALD processes. No iridium layer is used in these  
8 measurements, so the alloys themselves are functioning as the working electrode. The HP2P  
9 splitting is low and relatively constant for 21-46% Ru alloys. The HP2P increases dramatically  
10 when the alloy composition drops to 16 % Ru at all thicknesses.  
11  
12  
13  
14  
15  
16  
17  
18  
19  
20  
21  
22  
23

24 As shown in **Figure 6B**, however, the addition of an iridium layer significantly reduces the  
25 HP2P of TiO<sub>2</sub>-RuO<sub>2</sub> alloys with  $\leq 16\%$  Ru. This suggests that the increase in HP2P splitting  
26 observed when no iridium layer is used is most likely caused by insufficient Ru coverage at the  
27 surface to mediate efficient charge transfer to the ferri/ferrocyanide redox couple, and not by  
28 increased bulk resistivity of the alloy film. A metal layer is necessary to provide mediating  
29 electronic states at the electrolyte interface.<sup>1</sup> Without such a layer present, no observable  
30 Fe(II)/Fe(III) redox waves are observed (**Figure 5**, light blue dashed).<sup>1</sup> The increased HP2P  
31 splitting observed for low % Ru alloys is an intermediate case between these two extremes.  
32 Depositing a metal layer restores sufficient density of states at the electrode surface to mediate  
33 charge transfer, and Ru ions facilitate hole conduction through the bulk of the film. TiO<sub>2</sub>-RuO<sub>2</sub>  
34 films with only 13% RuO<sub>2</sub> do not contribute significant series resistance when a top metal  
35 contact is used.  
36  
37  
38  
39  
40  
41  
42  
43  
44  
45  
46  
47  
48  
49  
50  
51  
52  
53  
54  
55  
56  
57  
58  
59  
60

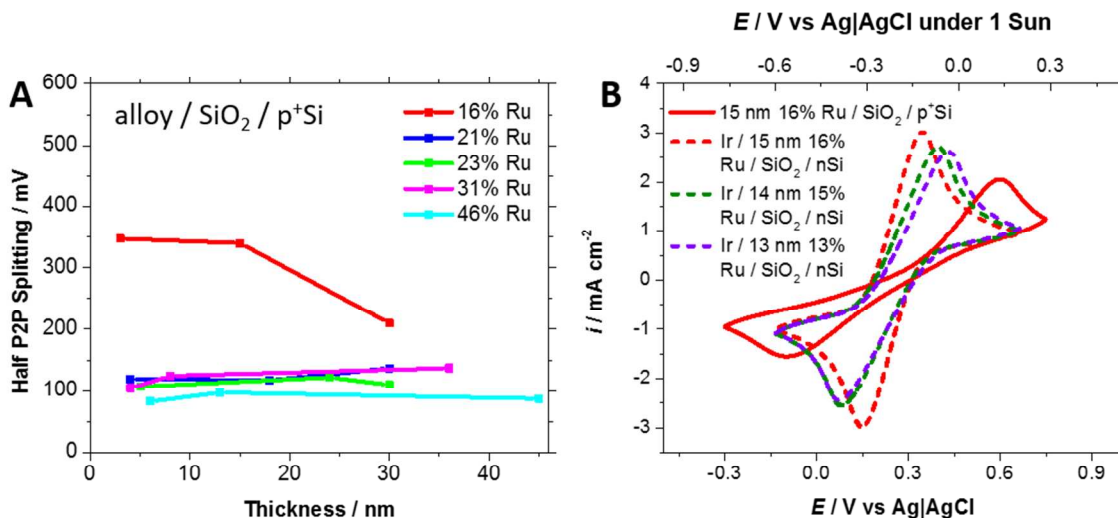


**Figure 6.** (A) Half peak-to-peak splitting (HP2P) for TiO<sub>2</sub>-RuO<sub>2</sub> alloys as a function of film thickness for compositions ranging from 16-46% Ru. All alloys were grown on p<sup>+</sup>Si, and the HP2P was measured in 10 mM ferri/ferrocyanide, 1 M KCl (B) Cyclic voltammograms comparing TiO<sub>2</sub>-RuO<sub>2</sub> alloy films with and without the presence of an iridium overlayer. The alloy sample measured without iridium was deposited on p<sup>+</sup>Si and is plotted with respect to the bottom x-axis. The alloy samples measured with iridium were deposited on nSi and are plotted with respect to the top x-axis. The total range of both axes are the same, and the max/min values were chosen to place the center of each voltammogram in the same location (since the nSi devices are shifted to negative potentials due to the photovoltage). The HP2P was again measured in 10 mM ferri/ferrocyanide, 1 M KCl, and the nSi measurements were performed under 1.5 AMG 1 sun illumination.

Overall, these electrochemical results demonstrate that TiO<sub>2</sub>-RuO<sub>2</sub> alloys are highly conductive. At higher Ru concentrations, they behave like metallic conductors. As the Ru concentration

1  
2  
3 decreases, they begin to lack sufficient density of states to mediate charge transfer at the surface  
4  
5 but are not sources of significant bulk series resistance.  
6  
7  
8  
9

### 10 11 2.3 HIGHLY CONDUCTIVE TiO<sub>2</sub>-RuO<sub>2</sub> ALLOY CONTACTS ENABLE HIGH 12 13 PHOTOVOLTAGE 14

15  
16  
17 Electrochemical measurements in ferri/ferrocyanide were performed to determine whether TiO<sub>2</sub>-  
18 RuO<sub>2</sub> alloy Schottky contacts would enable high photovoltages. **Figure 7A** shows cyclic  
19 voltammetry data for a representative Ir/TiO<sub>2</sub>-RuO<sub>2</sub> alloy/SiO<sub>2</sub>/nSi anode in AM1.5 light  
20 compared to a Ir/TiO<sub>2</sub>-RuO<sub>2</sub> alloy/SiO<sub>2</sub>/p<sup>+</sup>Si anode in the dark. All samples possess a native SiO<sub>2</sub>  
21 of approximately 2 nm in thickness, as measured by ellipsometry. The dashed line indicates the  
22 average E<sub>1/2</sub> across all 8 samples measured in the series. The box centered about the dashed line  
23 represents the variation in E<sub>1/2</sub> at the 95% confidence interval. All samples exhibit large  
24 photovoltages averaging 525 mV. The maximum photovoltage recorded was 549 mV for a 36  
25 nm 31% RuO<sub>2</sub> alloy, and the minimum photovoltage recorded was 489 mV for a 13 nm 46%  
26 RuO<sub>2</sub> alloy. Similar photovoltages were obtained without the iridium catalyst layer, as shown in  
27 **Figure 7B**. This confirms that the built-in field, which controls the photovoltage, is set by the  
28 TiO<sub>2</sub>-RuO<sub>2</sub> alloy, and not by the catalyst layer.  
29  
30  
31  
32  
33  
34  
35  
36  
37  
38  
39  
40  
41  
42  
43  
44  
45  
46  
47  
48  
49  
50  
51  
52  
53  
54  
55  
56  
57  
58  
59  
60

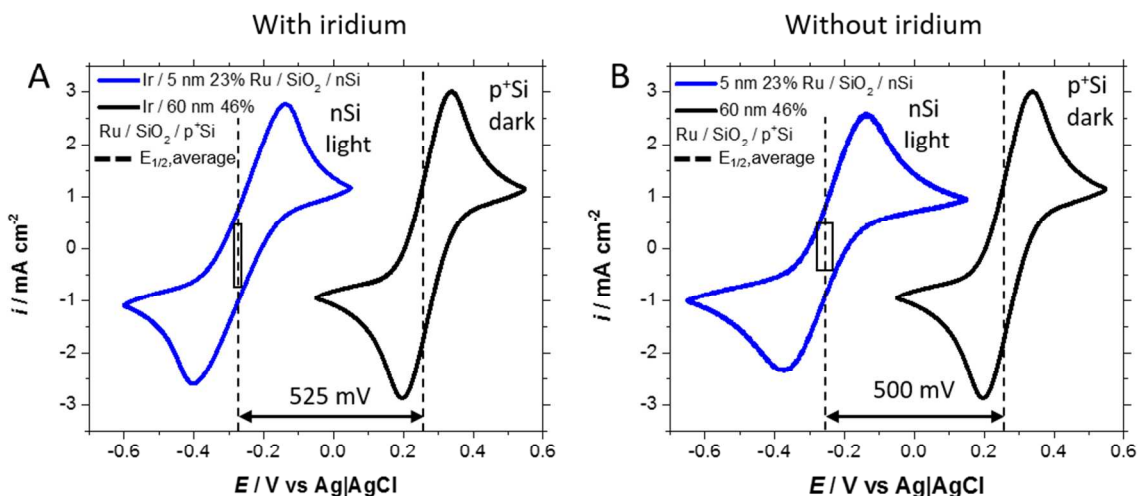
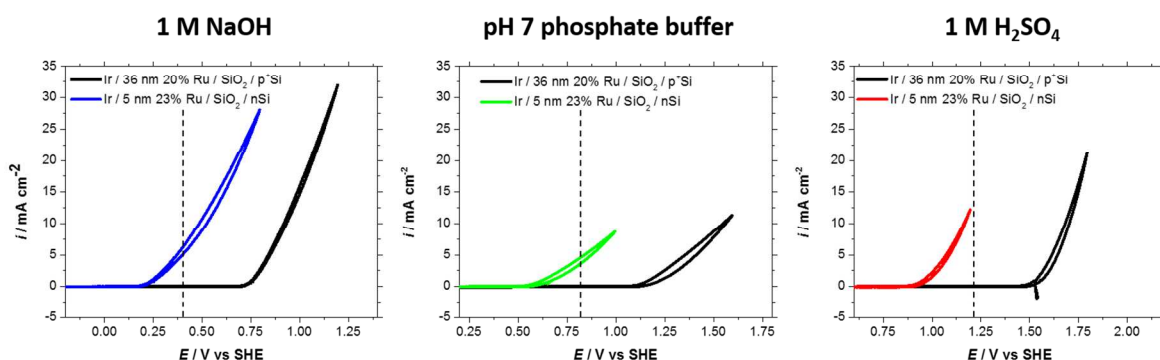


**Figure 7.** (A) Electrochemical performance of Ir/TiO<sub>2</sub>-RuO<sub>2</sub>/SiO<sub>2</sub>/n-Si anodes in one sun AM1.5 light compared to Ir/TiO<sub>2</sub>-RuO<sub>2</sub>/SiO<sub>2</sub>/p<sup>+</sup>-Si anode in the dark. (B) Electrochemical performance of TiO<sub>2</sub>-RuO<sub>2</sub>/SiO<sub>2</sub>/n-Si anodes in one sun AM1.5 light without the iridium catalyst compared to the Ir/TiO<sub>2</sub>-RuO<sub>2</sub>/SiO<sub>2</sub>/p<sup>+</sup>-Si anode in the dark. The dashed lines indicate the average  $E_{1/2}$  across all samples. The box centered about the dashed line represents the variation in  $E_{1/2}$  at the 95% confidence interval. The photovoltage for each nSi anode was calculated by comparing the  $E_{1/2}$  of the p<sup>+</sup>Si anode in the dark to the  $E_{1/2}$  of the nSi anode in the light. The average photovoltage across the series was calculated to be 525 mV with iridium and 500 mV without iridium.



1  
2  
3 **Figure 8.** Water oxidation curves in 1M NaOH, pH 7 phosphate buffer, and 1 M H<sub>2</sub>SO<sub>4</sub> for a  
4 representative Ir/TiO<sub>2</sub>-RuO<sub>2</sub> alloy/SiO<sub>2</sub>/nSi photoanode under 1 sun AM1.5 illumination  
5 compared to the analogous p<sup>+</sup>Si anode measured in the dark.  
6  
7  
8  
9

10  
11  
12  
13 The corresponding water oxidation data for Ir/TiO<sub>2</sub>-RuO<sub>2</sub>/SiO<sub>2</sub>/n-Si under 1 sun AM1.5  
14 illumination are shown in **Figure 8**. In different pH solutions, similar average photovoltages are  
15 observed during water oxidation at 1 mA cm<sup>-2</sup>: 504 mV ± 21 mV in 1 M NaOH, 534 mV ± 38  
16 mV in pH 7 phosphate buffer, and 539 mV ± 25 mV in 1 M H<sub>2</sub>SO<sub>4</sub> for all eight samples in the  
17 series. Water oxidation data with saturated photocurrent are shown in **Figure S14**.  
18  
19  
20  
21  
22  
23  
24  
25

26  
27  
28 To confirm the performance of TiO<sub>2</sub>-RuO<sub>2</sub> alloys as high work function, metallic Schottky  
29 contacts, capacitance voltage (CV) analysis of solid state capacitor structures was used to extract  
30 the work function for various alloy compositions. **Figure 9A** shows the structure of n and p-type  
31 MOS capacitors fabricated for this study. Aluminum, which has a reported work function of 4.1-  
32 4.2 eV,<sup>20</sup> was chosen as the gate metal for both n and pSi capacitors. The flatband voltage is  
33 determined by the difference between the metal and semiconductor work function, taking fixed  
34 charges, mobile charges, and interface traps into account.<sup>40</sup> When no TiO<sub>2</sub>-RuO<sub>2</sub> alloy is present  
35 in the MIS structure, the flatband voltage should be set by the work function of the aluminum top  
36 electrode. When ALD-grown alloys are introduced, however, the flatband voltage should reflect  
37 the work function of the conductive alloy film. As a high work function ( $\phi_M$ ) is expected for the  
38 TiO<sub>2</sub>-RuO<sub>2</sub> alloy, the flatband voltage should shift to more positive gate bias when such an alloy  
39 film is introduced into the capacitor stack, indicating a higher  $\phi_M$ . **Figures 9B** and **9C** show that  
40  
41  
42  
43  
44  
45  
46  
47  
48  
49  
50  
51  
52  
53  
54  
55  
56  
57  
58  
59  
60

such a shift is indeed observed. The flatband voltage shifts to higher gate bias by 0.7 V on pSi and 0.8 V on nSi.

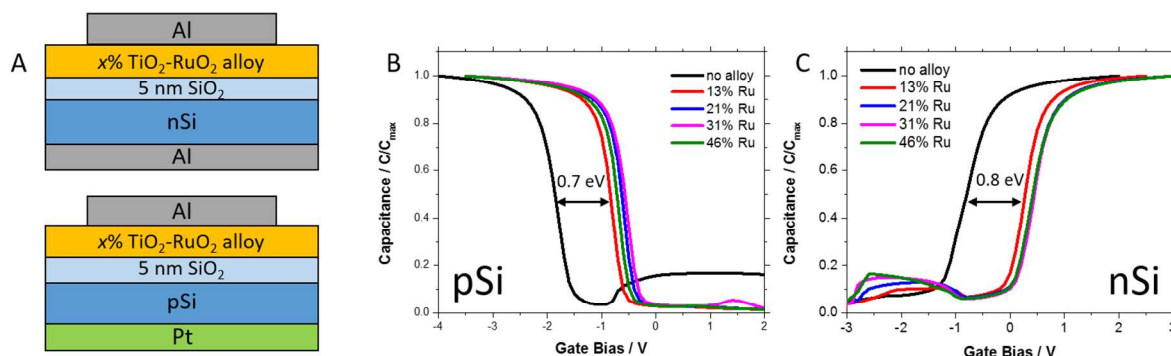


**Figure 9.** (A) Structure of n and pSi MOS capacitors. Aluminum was used as the gate metal in all cases. Aluminum and platinum were used to make Ohmic contacts to the back side of n and pSi substrates, respectively. (B) Capacitance-voltage (CV) curves for pSi MOS capacitors. (C) CV curves for nSi MOS capacitors. All CV curves were measured at a frequency of 1 MHz. The aluminum electrode dot diameter was 250  $\mu\text{m}$ . Since the alloys are highly conductive, the Al metal does not always define the capacitor area. As a result, the measured capacitance has been scaled to 1 for clarity. More detailed analysis of the CV curves is presented in the Supporting Information.

The work function of the  $\text{TiO}_2\text{-RuO}_2$  alloys was calculated from the observed flatband voltages. The details of these calculations are described in the Supporting Information, but briefly, the amount of fixed charge in the  $\text{SiO}_2$  was extracted from control samples with the structure Al / 5 nm  $\text{SiO}_2$  / Si capacitors, using an Al work function of 4.1 eV. Assuming that the ALD process does not affect the fixed oxide charge density in the  $\text{SiO}_2$ , the work functions of  $\text{TiO}_2\text{-RuO}_2$  alloy layers ranging from 16-46% Ru were calculated to be 5-5.2 eV. These values are reported in

**Table 2.**

**Table 2:** Calculated work function of TiO<sub>2</sub>-RuO<sub>2</sub> alloys of varying % Ru deposited on n and pSi with 5 nm thermally grown SiO<sub>2</sub>.

% Ru	$\phi_M$ on pSi	$\phi_M$ on nSi
0	4.08 (Al)	4.08 (Al)
13	5.05	5.11
21	5.19	5.20
31	5.26	5.26
46	5.28	5.21

The TiO<sub>2</sub>-RuO<sub>2</sub> alloys exhibit a work function in the same range as reported for RuO<sub>2</sub>. The work function of fully stoichiometric RuO<sub>2</sub> is reported to be > 5.0 eV.<sup>41,42</sup> It is also highly sensitive to the Ru oxidation state. In many cases, low temperature oxygen anneals are used to increase the work function.<sup>41</sup> Annealing under more reducing conditions has been shown to decrease the work function, either by formation of hydroxyls at the interface<sup>43,44</sup> or by complete reduction of RuO<sub>2</sub> back to Ru.<sup>41</sup> In the ALD-grown alloy layers, we hypothesize that depositing TiO<sub>2</sub> concurrently with Ru may favor the deposition of RuO<sub>2</sub> over metallic Ru by providing a more oxygen-rich environment. In addition to its high work function, RuO<sub>2</sub> is also a conductive oxide. It has a low resistivity of  $35.2 \pm 0.5 \mu\Omega \text{ cm}$  at room temperature.<sup>45</sup> Thus, TiO<sub>2</sub>-RuO<sub>2</sub> alloys can simultaneously achieve both high conductivity and high photovoltage.



For the composition range explored in this study, the work function does not seem to strongly depend on % Ru. Alloy work functions that are independent of composition have previously been attributed to some degree of surface phase segregation between the components.<sup>46</sup> For example, in the Cu-Ni system, a linear dependence of the work function on % Cu is only observed after sputter removal of the surface layers. However, the photovoltage obtained from these TiO<sub>2</sub>-RuO<sub>2</sub> alloys shows no measurable dependence on % Ru, indicating that the work function does not vary significantly over the composition range investigated. Further experiments at lower % Ru are necessary to fully characterize the effect of composition on the work function and conductivity of these amorphous ALD-grown TiO<sub>2</sub>-RuO<sub>2</sub> alloys.

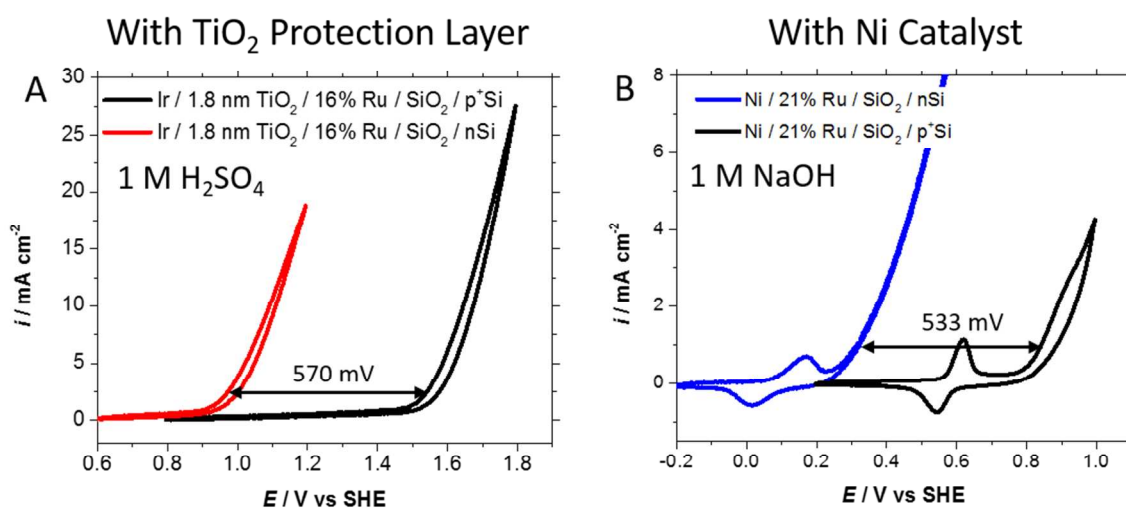


**Figure 10.** (A) Representative water oxidation data in 1 M H<sub>2</sub>SO<sub>4</sub> for nSi samples in the light compared to p<sup>+</sup>Si samples in the dark in which a 1.8 nm TiO<sub>2</sub> protection layer has been incorporated above the 10 nm 21% Ru alloy layer. The photovoltage is indicated at 2 mA/cm<sup>2</sup> for clarity. (B) Representative water oxidation data in 1 M NaOH for nSi samples in the light compared to p<sup>+</sup>Si samples in the dark using a nickel catalyst on a 10 nm 21% Ru alloy. The photovoltage is indicated at 1 mA/cm<sup>2</sup>.

1  
2  
3  
4  
5  
6 Because the work function is set by the TiO<sub>2</sub>-RuO<sub>2</sub> alloy film, the photovoltage of the resulting  
7  
8 MIS Schottky junctions does not change when a TiO<sub>2</sub> protection layer is incorporated or when  
9  
10 the surface catalyst identity is changed. **Figure 10A** shows water oxidation data in 1 M H<sub>2</sub>SO<sub>4</sub>  
11  
12 for nSi photoanodes tested in the light compared to p<sup>+</sup>Si photoanodes in the dark in which a 1.8  
13  
14 nm TiO<sub>2</sub> protection layer was deposited on top of the TiO<sub>2</sub>-RuO<sub>2</sub> alloy layer. TiO<sub>2</sub> overlayer  
15  
16 thickness was calculated from XPS measurements based on the attenuation of the Ru 3d peak  
17  
18 originating from the alloy by the TiO<sub>2</sub> overlayer (**Figure S15**). At 2 mA/cm<sup>2</sup> (chosen for clarity  
19  
20 in the figure), the photovoltage is still 570 mV. The average photovoltage measured in FFC was  
21  
22 560 mV. This represents a 170-390 mV enhancement in photovoltage compared to previous  
23  
24 studies using highly conductive TiO<sub>2</sub>.<sup>2,13</sup> Because 2 nm TiO<sub>2</sub> is simply a tunnel barrier,<sup>11</sup> its  
25  
26 incorporation does not increase the half peak-to-peak splitting in FFC (**Figure S16**). RuO<sub>2</sub> is  
27  
28 known to form soluble Ru(VIII) products at more positive potentials,<sup>15</sup> and incorporation of a  
29  
30 TiO<sub>2</sub> protection layer would likely be necessary for long-term operation. Although extended  
31  
32 stability tests are outside the scope of this work, 2 nm ALD TiO<sub>2</sub> has been shown to sufficiently  
33  
34 protect silicon photoanodes during water oxidation.<sup>1</sup> **Figure 10B** shows water oxidation data in 1  
35  
36 M NaOH for nSi photoanodes tested in the light compared to p<sup>+</sup>Si photoanodes in the dark using  
37  
38 ultrathin evaporated nickel films as the oxygen evolution catalyst. Eight samples were tested  
39  
40 using alloy films ranging from 21% to 46% Ru and film thicknesses ranging from 3-45 nm. The  
41  
42 average photovoltage was 533 mV ± 33 mV at the 95% confidence interval. Thus, isolating the  
43  
44 MIS junction using TiO<sub>2</sub>-RuO<sub>2</sub> alloys enables high photovoltages irrespective of catalyst identity  
45  
46 or incorporation of metal oxide protection layers.  
47  
48  
49  
50  
51  
52  
53  
54

### 55 3. CONCLUSIONS

56  
57  
58  
59  
60

1  
2  
3 We have demonstrated that ALD alloys of TiO<sub>2</sub> and RuO<sub>2</sub> with compositions as low as  
4  
5 13% Ru can be used to set the built-in field, and hence control the photovoltage, in silicon  
6  
7 MIS photoanodes. Photovoltages above 500 mV were consistently achieved regardless of  
8  
9 catalyst identity, presence of TiO<sub>2</sub> protection layers, alloy film thickness, or alloy  
10  
11 composition. Average photovoltages of 533 mV were achieved for as-deposited anodes  
12  
13 using a NiO<sub>x</sub> catalyst, a significant improvement over the 180-400 mV photovoltages  
14  
15 previously reported for silicon photoanodes without a buried p<sup>+</sup>n homojunction. Isolating  
16  
17 the MIS Schottky junction effectively creates an isolated photovoltaic cell in series with  
18  
19 an efficient water oxidation catalyst. As a result, this is a promising strategy for  
20  
21 maximizing the photovoltage in silicon MIS devices, and additional components can now  
22  
23 be incorporated and optimized without sacrificing the photovoltage. In addition, the  
24  
25 conductivity and work function of these alloy contacts can, in principle, be tailored for  
26  
27 other semiconductors, particularly those which do not form high quality buried  
28  
29 homojunctions. This work suggests that a range of conductive metal oxide Schottky  
30  
31 contacts can be synthesized by ALD alloying.  
32  
33  
34  
35  
36  
37  
38  
39  
40

## 41 4. EXPERIMENTAL

### 42 4.1. Silicon substrates

43  
44 Heavily boron-doped (100) p-type silicon wafers ( $\rho = 0.001\text{-}0.002 \text{ } \Omega \text{ cm}$ , thickness 505-545  $\mu\text{m}$ )  
45  
46 were used as conductive silicon substrates for electrochemical measurements in the dark.  
47  
48 Moderately phosphorous-doped (100) n-type silicon wafers ( $\rho = 0.14\text{-}0.24 \text{ } \Omega \text{ cm}$ , thickness 450  
49  
50  $\mu\text{m}$ ) were used for electrochemical measurements in the light. The wafers were used as-received  
51  
52 with a 1.5-2 nm native SiO<sub>2</sub> layer, as measured by ellipsometry. MOS capacitors for CV analysis  
53  
54  
55  
56  
57  
58  
59  
60

1  
2  
3 were fabricated on moderately boron-doped (100) p-type silicon wafers ( $\rho = 1-10 \text{ } \Omega \text{ cm}$ ,  
4 thickness 500-550  $\mu\text{m}$ ) with 50  $\text{Å}$  dry thermal oxide and on moderately phosphorous-doped  
5  
6 (100) n-type silicon wafers ( $\rho = 0.20-0.40 \text{ } \Omega \text{ cm}$ , thickness 500-550  $\mu\text{m}$ ) with 50  $\text{Å}$  dry thermal  
7  
8 oxide.  
9  
10

#### 11 12 13 14 15 4.2 Atomic Layer Deposition (ALD)

16  
17 All ALD films were deposited in a custom-built ALD reactor (**Figure S1**).  
18 Tetrakis(dimethylamido)titanium (TDMAT) was used as the metal precursor and water as the co-  
19 reactant.<sup>47</sup> The TDMAT bubbler was kept at 60 °C (oven temperature) and the water bubbler was  
20 kept at room temperature. The substrate temperature was approximately 175 °C, within the ALD  
21 window for the TDMAT system.<sup>21,47</sup> The precursor pulse sequence is described in the Table S1  
22 of the Supporting Information, but briefly, the TDMAT pulse time was 3 s and the H<sub>2</sub>O pulse  
23 time was 0.5 s. TDMAT was pulsed into a stream of N<sub>2</sub> carrier gas at 50 sccm, but N<sub>2</sub> gas was  
24 not flowed through the TDMAT bubbler itself. N<sub>2</sub> at 50 sccm was also used as the purge gas.  
25 The equilibrium deposition pressure was approximately 300 mTorr. The TDMAT growth rate  
26 saturates as a function of precursor pulse time (**Figure S2**), a hallmark of ALD growth.  
27  
28  
29  
30  
31  
32  
33  
34  
35  
36  
37  
38  
39  
40  
41  
42

43 RuO<sub>x</sub> films were grown using bis(2,4-dimethylpentadienyl) ruthenium (Ru(DMPD)<sub>2</sub>) and  
44 oxygen. This precursor was chosen because its low temperature ALD window overlaps with that  
45 of TDMAT.<sup>22,23</sup> The Ru(DMPD)<sub>2</sub> bubbler was kept at 60 °C (oven temperature), and the  
46 deposition temperature was 175 °C. Ru(DMPD)<sub>2</sub> is a solid with a lower vapor pressure than  
47 TDMAT, so N<sub>2</sub> at 50 sccm was used as a carrier gas through the bubbler. N<sub>2</sub> at 50 sccm was also  
48 used as the purge gas. The equilibrium deposition pressure was approximately 300 mTorr. The  
49  
50  
51  
52  
53  
54  
55  
56  
57  
58  
59  
60

1  
2  
3 precursor pulse sequence is described in Table S2 of the Supporting Information, but briefly, the  
4  
5 Ru(DMPD)<sub>2</sub> pulse time was 60 s and the O<sub>2</sub> pulse time was 30 s.  
6  
7  
8  
9

10 To grow TiO<sub>2</sub>-RuO<sub>2</sub> alloys, alternating cycles of TiO<sub>2</sub> and RuO<sub>x</sub> were repeated for a specified  
11  
12 number of super-cycles. The ratio of TiO<sub>2</sub> cycles to RuO<sub>x</sub> cycles was varied to control the Ru  
13  
14 content in the film. The number of super-cycles was varied to control the film thickness. All  
15  
16 deposition conditions were the same as the individual ALD processes.  
17  
18  
19  
20  
21

#### 22 4.3 Determination of TiO<sub>2</sub> Thickness by Ellipsometry

23  
24 TiO<sub>2</sub> thickness was measured using a Gaertner ellipsometer calibrated by cross-sectional  
25  
26 transmission electron microscopy (TEM) analysis. Each sample was approximately 2 x 2 cm,  
27  
28 based on the diameter of the deposition chamber and the ceramic heater's zone of uniformity. 9  
29  
30 points were typically measured on each sample and 95% confidence intervals were calculated for  
31  
32 the mean thickness. After optimizing the TiO<sub>2</sub> depositions, a typical 6 nm film had a thickness  
33  
34 range of 6.5 – 6.8 nm and a variation of 0.06 nm at the 95% confidence interval. A typical 12 nm  
35  
36 film had a thickness range of 11.6 – 11.9 nm and a variation of 0.07 nm at the 95% confidence  
37  
38 interval.  
39  
40  
41  
42  
43  
44  
45

#### 46 4.4 Determination of Alloy Film Thickness by X-Ray Reflectivity (XRR)

47  
48 Alloy film thickness was measured by X-Ray Reflectivity using a PANalytical X'Pert  
49  
50 Diffractometer. The incident beam optics included a graded multilayer parabolic X-ray mirror, a  
51  
52 1/32° divergence slit, a 10 mm mask for smaller samples, and a Ni 0.15 mm automatic beam  
53  
54 attenuator. The diffracted beam optics included a parallel plate collimator with a 0.27° receiving  
55  
56  
57  
58  
59  
60

1  
2  
3 slit. PANalytical's X'Pert Reflectivity software was used to calculate film thickness from a  
4  
5  
6 2Theta-Omega scan using the Fourier transform method. Scans were collected from 0-8° 2θ. The  
7  
8 step size was 0.02° and the time per step was 0.2 s.  
9

#### 10 11 12 13 4.5 Determination of crystal structure by grazing incidence X-ray diffraction (GIXRD)

14  
15 GIXRD spectra were collected on a PANalytical X'Pert Diffractometer. The incident beam  
16  
17 optics included a graded multilayer parabolic X-ray mirror, a 1/2° divergence slit, a 15 mm mask  
18  
19 for smaller samples, and a Ni 0.15 mm automatic beam attenuator. The diffracted beam optics  
20  
21 included a parallel plate collimator. No receiving slit was used in order to maximize the signal  
22  
23 intensity. Scans were collected from 20-80° 2θ with  $\omega = 2.5^\circ$ . The step size was 0.05° with a  
24  
25 time per step of 1 s.  
26  
27  
28  
29  
30  
31

#### 32 4.6 Deposition of catalyst, gate metal, and back-contact

33  
34 Iridium, aluminum, and platinum were deposited by electron beam evaporation. For the MOS  
35  
36 capacitor studies, 100 nm of Al and 20 nm of Pt was used. Al was used as the gate metal for both  
37  
38 n and p-Si wafers. Al was used as the back contact for n-Si wafers, and Pt was used as the back  
39  
40 contact for p-Si wafers. For the electrochemical measurements, 2 nm Ir, 100 nm Al, and 20 nm  
41  
42 Pt were used. Again, Al was used as the back contact for all n-Si wafers, and Pt was used as the  
43  
44 back contact for al p<sup>+</sup>-Si wafers.  
45  
46  
47  
48  
49  
50

#### 51 4.7 X-Ray Photoelectron Spectroscopy (XPS)

52  
53 Elemental characterization of the alloy films was performed using a PHI 5000 VersaProbe™ X-  
54  
55 Ray Photoelectron Spectrometer. The chamber base pressure was typically on the order of 10<sup>-7</sup>  
56  
57  
58  
59  
60

1  
2  
3 Torr. The X-ray source was monochromatic Al K $\alpha$  (1486.6 eV). The X-ray power was 50 W,  
4  
5 and the beam diameter was focused to 200  $\mu\text{m}$ . The source-analyzer angle was 45°. For survey  
6  
7 scans, the pass energy was 117.4 eV with an energy step of 1.0 eV. For high resolution scans, the  
8  
9 pass energy was 23.5 eV with an energy step of 0.10 eV. The time/step was 20 ms in all cases.  
10  
11

12  
13  
14 CasaXPS software was used for all elemental analyses and peak fitting procedures. All peak  
15  
16 positions were referenced to the Si 2p peak at 99 eV. Relative sensitivity factors for each element  
17  
18 were taken from the PHI Multipak Manual.  
19  
20  
21

#### 22 23 24 4.8 Electrochemical Measurements 25 26

27 The pH 7 phosphate buffer solution was made with 0.42 M Na<sub>2</sub>HPO<sub>4</sub> and 0.58 M NaH<sub>2</sub>PO<sub>4</sub>. The  
28  
29 pH was measured and adjusted accordingly to 7. The acidic and basic solutions were made with  
30  
31 1 M H<sub>2</sub>SO<sub>4</sub> and 1 M NaOH, respectively. The aqueous ferri/ferrocyanide solution was made with  
32  
33 10 mM K<sub>3</sub>Fe(CN)<sub>6</sub>, 10 mM K<sub>4</sub>Fe(CN)<sub>6</sub>, and 1 M KCl. All electrochemical measurements were  
34  
35 performed using a bored (5 mm diameter, 0.196 cm<sup>2</sup> area) Teflon cone pressed against the  
36  
37 sample to define the electrode area and contain the electrolyte solution. A Pt wire was used as a  
38  
39 counter electrode. A Ag(s)|AgCl(s) sat. KCl (aq) electrode purchased from BioAnalytical  
40  
41 Systems was used as the reference electrode. Potentials measured versus Ag|AgCl were  
42  
43 converted to SHE. All measurements were conducted using a WaveNow potentiostat in air at  
44  
45 room temperature. Cyclic voltammograms were recorded at a scan rate of 100 mV s<sup>-1</sup>.  
46  
47  
48 Chronoamperometry stability measurements were performed using a peristaltic pump to circulate  
49  
50 the solution at 1 mL s<sup>-1</sup>.  
51  
52  
53  
54  
55  
56  
57  
58  
59  
60

#### 4.9 MOS Capacitor Fabrication and Measurements

MOS capacitors were fabricated using stencil lithography. Al gate metals were deposited through a shadow mask that defined circular capacitors of diameters ranging from 100-250  $\mu\text{m}$ . All CV measurements were taken at room temperature. The gate bias was varied such that the capacitors moved from depletion to accumulation. A superimposed 25 mV AC voltage was applied at a frequency range of 1 kHz – 1 MHz.

#### 4.10 Auger Electron Spectroscopy (AES) Mapping

AES maps were collected using a PHI 700 Auger Electron Spectrometer. For high resolution maps, a beam energy of 10 kV with 10 nA was chosen. A 2-point acquisition method was used with a resolution of 256 pixels.

#### 4.11 Ultra-violet visible Spectroscopy (UV-vis)

UV-vis spectra were collected on a Cary 6000i UV/Vis/NIR Spectrometer in the wavelength range 200-1800 nm. A bare quartz slide was used for baseline correction. Fused quartz slides of thickness 1 mm were purchased from AdValue Technology.

#### 4.12 Transmission Electron Microscopy (TEM)

Micro-structural analysis was performed using an HR-TEM (Jeol 2100 transmission electron microscope; 200 kV; double tilt holder). Cross-sections of the films were prepared using a FEI Dual-Beam Helios NanoLab 600i Focused Ion Beam (FIB) (final thinning at 93 pA 30 kV, final polish 5 kV 47 pA).



1  
2  
3 ASSOCIATED CONTENT  
4  
5

6 Supporting Information: Detailed methods and analysis for XPS, XRR, GIXRD, UV-vis,  
7 capacitance-voltage analysis, AES, and TEM. Also contains a detailed description of custom  
8  
9 ALD reactor. This material is available free of charge via the Internet at <http://pubs.acs.org>.  
10  
11  
12  
13

14  
15  
16  
17 AUTHOR INFORMATION  
18

19  
20 **Corresponding Author**  
21

22 \*C. E. D. Chidsey. Email: [chidsey@stanford.edu](mailto:chidsey@stanford.edu)  
23  
24

25 \*P. C. McIntyre. Email: [pcm1@stanford.edu](mailto:pcm1@stanford.edu)  
26  
27

28  
29 **Author Contributions**  
30

31 O. H. prepared all samples and performed all experiments for this study with the aid of A. S. M.  
32 S. prepared and imaged alloy samples by transmission electron microscopy. O. H., C. E. D. C.,  
33 P. H., and P. M. designed the experiments. All authors helped in the preparation of this  
34 manuscript.  
35  
36

37 **Notes**  
38

39 The authors declare no competing financial interest.  
40  
41  
42

43  
44 ACKNOWLEDGMENTS  
45

46 We thank T. Carver for metal e-beam evaporations and all members of the RENEW  
47 collaboration in addition to the authors: M. Pemble, A. Mills, I. Povey, J. Kegel, K. Cherkaoui,  
48 S. Monaghan, and D. Hazafy. O. H. would like to thank McIntyre group members A.  
49 Scheuermann, K. Kemp, R. Tang-Kong, A. Negara, T. Chor Seng, and W. Tang, as well as  
50  
51 Chidsey group members S. Ramakrishnan and M. Van den Berg for insightful discussions. O. H.  
52  
53  
54  
55  
56  
57  
58  
59  
60

1  
2  
3 would also like to thank C. Hitzman of the Stanford Nano Shared Facilities for his guidance with  
4 XPS and AES. We also acknowledge A. Vailionis for his help with XRR and GIXRD  
5 measurements. This work was partially supported by the Stanford Global Climate and Energy  
6 Project and National Science Foundation program CBET-1336844. The authors from Tyndall  
7 National Institute acknowledge the financial support of Science Foundation (SFI) under the US-  
8 Ireland R&D Partnership Program—Grant Number SFI/13/US/12543. O. H. graciously  
9 acknowledges support from the Fannie and John Hertz Foundation.  
10  
11  
12  
13  
14  
15  
16  
17  
18  
19

## 20 REFERENCES

- 21  
22  
23 (1) Chen, Y. W.; Prange, J. D.; Dühnen, S.; Park, Y.; Gunji, M.; Chidsey, C. E. D.; McIntyre,  
24 P. C. Atomic Layer-Deposited Tunnel Oxide Stabilizes Silicon Photoanodes for Water  
25 Oxidation. *Nat. Mater.* **2011**, *10* (7), 539–544.  
26  
27  
28  
29  
30  
31 (2) Hu, S.; Shaner, M. R.; Beardslee, J. A.; Lichterman, M.; Brunschwig, B. S.; Lewis, N. S.  
32 Amorphous TiO<sub>2</sub> Coatings Stabilize Si, GaAs, and GaP Photoanodes for Efficient Water  
33 Oxidation. *Science* **2014**, *344*, 1005–1009.  
34  
35  
36  
37  
38  
39 (3) Singh, R.; Green, M. A.; Rajkanan, K. Review of Conductor-Insulator-Semiconductor  
40 (CIS) Solar Cells. *Sol. Cells* **1981**, *3* (2), 95–148.  
41  
42  
43  
44  
45 (4) Green, M. A. Effects of Pinholes, Oxide Traps, and Surface States on MIS Solar Cells.  
46 *Appl. Phys. Lett.* **1978**, *33* (2), 178–180.  
47  
48  
49  
50 (5) Green, M. a; Blakers, a W. Advantages of Metal-Insulator-Semiconductor Structure for  
51 Silicon Solar Cells. *Sol. Cells* **1983**, *8*, 3–16.  
52  
53  
54  
55  
56 (6) Godfrey, R. B.; Green, M. A. 655 mV Open-Circuit Voltage, 17.6% Efficient Silicon MIS  
57  
58  
59  
60

- 1  
2  
3 Solar Cells. *Appl. Phys. Lett.* **1979**, *34* (11), 790–793.  
4  
5  
6  
7 (7) Lichterman, M. F.; Sun, K.; Hu, S.; Zhou, X.; McDowell, M. T.; Shaner, M. R.; Richter,  
8 M. H.; Crumlin, E. J.; Carim, A. I.; Saadi, F. H.; Brunshwig, B. S.; Lewis, N. S.  
9 Protection of Inorganic Semiconductors for Sustained, Efficient Photoelectrochemical  
10 Water Oxidation. *Catal. Today* **2016**, *262*, 11–23.  
11  
12  
13  
14  
15  
16  
17 (8) Kenney, M. J.; Gong, M.; Li, Y.; Wu, J. Z.; Feng, J.; Lanza, M.; Dai, H. High-  
18 Performance Silicon Photoanodes Passivated with Ultrathin Nickel Films for Water  
19 Oxidation. *Science* **2013**, *342* (6160), 836–840.  
20  
21  
22  
23  
24  
25 (9) Shaner, M. R.; Hu, S.; Sun, K.; Lewis, N. S. Stabilization of Si Microwire Arrays for  
26 Solar-Driven H<sub>2</sub>O Oxidation to O<sub>2</sub>(g) in 1.0 M KOH(aq) Using Conformal Coatings of  
27 Amorphous TiO<sub>2</sub>. *Energy Environ. Sci.* **2015**, *8*, 203–207.  
28  
29  
30  
31  
32  
33 (10) Zhou, X.; Liu, R.; Sun, K.; Friedrich, D.; McDowell, M. T.; Yang, F.; Omelchenko, S. T.;  
34 Saadi, F. H.; Nielander, A. C.; Yalamanchili, S.; Papadantonakis, K. M.; Brunshwig, B.  
35 S.; Lewis, N. Interface Engineering of the Photoelectrochemical Performance of Ni-  
36 Oxide-Coated N-Si Photoanodes by Atomic-Layer Deposition of Ultrathin Films of  
37 Cobalt Oxide. *Energy Environ. Sci.* **2015**, *8*, 2644–2649.  
38  
39  
40  
41  
42  
43  
44  
45 (11) Scheuermann, A. G.; Prange, J. D.; Gunji, M.; Chidsey, C. E. D.; McIntyre, P. C. Effects  
46 of Catalyst Material and Atomic Layer Deposited TiO<sub>2</sub> Oxide Thickness on the Water  
47 Oxidation Performance of Metal–insulator–silicon Anodes. *Energy Environ. Sci.* **2013**, *6*  
48 (8), 2487–2496  
49  
50  
51  
52  
53  
54  
55  
56 (12) Scheuermann, A. G.; Lawrence, J. P.; Kemp, K. W.; Ito, T.; Walsh, A.; Chidsey, C. E. D.;  
57  
58  
59  
60

- 1  
2  
3 Hurley, P. K.; McIntyre, P. C. Design Principles for Maximizing Photovoltage in Metal-  
4 Oxide-Protected Water-Splitting Photoanodes. *Nat. Mater.* **2016**, *15* (October), 99–105.  
5  
6  
7  
8  
9 (13) McDowell, M. T.; Lichterman, M. F.; Carim, A. I.; Liu, R.; Hu, S.; Brunschwig, B. S.;  
10 Lewis, N. S. The Influence of Structure and Processing on the Behavior of TiO<sub>2</sub>  
11 Protective Layers for Stabilization of N-Si/TiO<sub>2</sub>/Ni Photoanodes for Water Oxidation.  
12 *ACS Appl. Mater. Interfaces* **2015**, *7* (28), 15189–15199.  
13  
14  
15  
16  
17  
18  
19 (14) Green, M. A. Limits on the Open-Circuit Voltage and Efficiency of Silicon Solar Cells  
20 Imposed by Intrinsic Auger Processes. *IEEE Trans. Electron Devices* **1984**, *ED-31* (5),  
21 671–678.  
22  
23  
24  
25  
26  
27 (15) Pourbaix, M. *Atlas of Electrochemical Equilibria in Aqueous Solutions*; 1966.  
28  
29  
30 (16) Trasatti, S. Electrocatalysis: Understanding the Success of DSA®. *Electrochim. Acta*  
31 **2000**, *45* (15-16), 2377–2385.  
32  
33  
34  
35  
36 (17) Over, H. Surface Chemistry of Ruthenium Dioxide in Heterogeneous Catalysis and  
37 Electrocatalysis: From Fundamental to Applied Research. *Chem. Rev.* **2012**, *112* (6),  
38 3356–3426.  
39  
40  
41  
42  
43  
44 (18) Trasatti, S. Physical Electrochemistry of Ceramic Oxides. *Electrochim. Acta* **1991**, *36* (2),  
45 225–241.  
46  
47  
48  
49 (19) Greiner, M. T.; Chai, L.; Helander, M. G.; Tang, W. M.; Lu, Z. H. Transition Metal Oxide  
50 Work Functions: The Influence of Cation Oxidation State and Oxygen Vacancies. *Adv.*  
51 *Funct. Mater.* **2012**, *22* (21), 4557–4568.  
52  
53  
54  
55  
56  
57 (20) Michaelson, H. B. The Work Function of the Elements and Its Periodicity. *J. Appl. Phys.*  
58  
59  
60

- 1  
2  
3 **1977**, 48 (11), 4729–4733.  
4  
5  
6  
7 (21) Scheuermann, A. G.; Lawrence, J. P.; Gunji, M.; Chidsey, C. E. D.; McIntyre, P. C. ALD-  
8 TiO<sub>2</sub> Preparation and Characterization for Metal-Insulator-Silicon Photoelectrochemical  
9 Applications. *ECS Trans.* **2013**, 58 (10), 75–86.  
10  
11  
12  
13  
14 (22) Methaapanon, R.; Geyer, S. M.; Lee, H.-B.-R.; Bent, S. F. The Low Temperature Atomic  
15 Layer Deposition of Ruthenium and the Effect of Oxygen Exposure. *J. Mater. Chem.*  
16 **2012**, 25154–25160.  
17  
18  
19  
20  
21  
22 (23) Methaapanon, R.; Geyer, S. Size Dependent Effects in Nucleation of Ru and Ru Oxide  
23 Thin Films by Atomic Layer Deposition Measured by Synchrotron Radiation X-Ray  
24 Diffraction. *Chem. Mater.* **2013**, 25, 3458–3463.  
25  
26  
27  
28  
29  
30 (24) Aaltonen, T.; Aløn, P.; Ritala, M.; Leskelä, M. Ruthenium Thin Films Grown by Atomic  
31 Layer Deposition. *Chem. Vap. Deposition* **2003**, 9 (1), 45–49.  
32  
33  
34  
35  
36 (25) Aaltonen, T.; Ritala, M.; Arstila, K.; Keinonen, J.; Leskelä, M. Atomic Layer Deposition  
37 of Ruthenium Thin Films from Ru(thd)<sub>3</sub> and Oxygen. *Chem. Vap. Deposition* **2004**, 10  
38 (4), 215–219.  
39  
40  
41  
42  
43  
44 (26) Li, H.; Aaltonen, T.; Li, Z.; Lim, B. S.; Gordon, R. G.; Rd, V. Synthesis and  
45 Characterization of Ruthenium Amidinate Complexes as Precursors for Vapor Deposition.  
46 *Open Inorg. Chem. J.* **2008**, 2, 11–17.  
47  
48  
49  
50  
51  
52 (27) Gregorczyk, K.; Henn-lecordier, L.; Gatineau, J.; Dussarrat, C.; Rubloff, G. Atomic Layer  
53 Deposition of Ruthenium Using the Novel Precursor bis(2,6,6-Trimethyl-  
54 Cyclohexadienyl)ruthenium. *Chem. Mater.* **2011**, 23, 2650–2656.  
55  
56  
57  
58  
59  
60

- 1  
2  
3  
4  
5  
6  
7  
8  
9  
10  
11  
12  
13  
14  
15  
16  
17  
18  
19  
20  
21  
22  
23  
24  
25  
26  
27  
28  
29  
30  
31  
32  
33  
34  
35  
36  
37  
38  
39  
40  
41  
42  
43  
44  
45  
46  
47  
48  
49  
50  
51  
52  
53  
54  
55  
56  
57  
58  
59  
60
- (28) Kim, S. K.; Lee, S. Y.; Lee, S. W.; Hwang, G. W.; Hwang, C. S.; Lee, J. W.; Jeong, J. Atomic Layer Deposition of Ru Thin Films Using 2,4-(Dimethylpentadienyl)(ethylcyclopentadienyl)Ru by a Liquid Injection System. *J. Electrochem. Soc.* **2007**, *154*, D95.
- (29) Diebold, U. TiO<sub>2</sub> by XPS. *Surf. Sci. Spectra* **1996**, *4* (3), 227.
- (30) Jensen, D. S.; Kanyal, S. S.; Madaan, N.; Vail, M. A.; Dadson, A. E.; Engelhard, M. H.; Linford, M. R. Silicon (100)/SiO<sub>2</sub> by XPS. *Surf. Sci. Spectra* **2013**, *20* (1), 36–42.
- (31) Morgan, D. J. Resolving Ruthenium: XPS Studies of Common Ruthenium Materials. *Surf. Interface Anal.* **2015**, *47* (11), 1072–1079.
- (32) Kaga, Y. Ru and RuO<sub>2</sub> Thin Films by XPS. *Surf. Sci. Spectra* **1999**, *6* (1), 68.
- (33) Kim, Y. J.; Gao, Y.; Chambers, S. a. Core-Level X-Ray Photoelectron Spectra and X-Ray Photoelectron Diffraction of RuO<sub>2</sub>(110) Grown by Molecular Beam Epitaxy on TiO<sub>2</sub>(110). *Appl. Surf. Sci.* **1997**, *120*, 250–260.
- (34) Mun, C.; Ehrhardt, J. J.; Lambert, J.; Madic, C. XPS Investigations of Ruthenium Deposited onto Representative Inner Surfaces of Nuclear Reactor Containment Buildings. *Appl. Surf. Sci.* **2007**, *253* (18), 7613–7621.
- (35) Oh, S.; Park, C.; Park, C. Thermal Stability of RuO<sub>2</sub>/Ru Bilayer Thin Film in Oxygen Atmosphere. *Thin Solid Films* **2000**, *359*, 118–123.
- (36) Todorova, M.; Li, W. X.; Ganduglia-Pirovano, M. V.; Stampfl, C.; Reuter, K.; Scheffler, M. Role of Subsurface Oxygen in Oxide Formation at Transition Metal Surfaces. *Phys. Rev. Lett.* **2002**, *89* (9), 096103.

- 1  
2  
3  
4 (37) Naslund, L.-A.; Sanchez-Sanchez, C. M.; Ingason, A. S.; Backstrom, J.; Herrero, E.;  
5  
6 Rosen, J.; Holmin, S. The Role of TiO<sub>2</sub> Doping on RuO<sub>2</sub> -Coated Electrodes for the  
7  
8 Water Oxidation Reaction. *J. Phys. Chem. C* **2013**, *117* (12), 6126–6135.  
9  
10  
11 (38) Islam, S. Z.; Reed, A.; Kim, D. Y.; Rankin, S. E. N<sub>2</sub>/Ar Plasma Induced Doping of  
12  
13 Ordered Mesoporous TiO<sub>2</sub> Thin Films for Visible Light Active Photocatalysis.  
14  
15 *Microporous Mesoporous Mater.* **2016**, *220*, 120–128.  
16  
17  
18 (39) Asahi, R.; Morikawa, T.; Ohwaki, T.; Aoki, K.; Taga, Y. Visible-Light Photocatalysis in  
19  
20 Nitrogen-Doped Titanium Oxides. *Science* **2001**, *293*, 269–272.  
21  
22  
23 (40) Schroder, D. K. Electrical Characterization of Defects in Gate Dielectrics. In *Defects in*  
24  
25 *Microelectronic Materials and Devices*; Fleetwood, D. M., Pantelides, S. T., Schrimpf, R.  
26  
27 D., Eds.; CRC Press, 2009.  
28  
29  
30  
31 (41) Park, C. S.; Bersuker, G.; Hung, P. Y.; Kirsch, P. D.; Jammy, R. Impact of Oxygen on  
32  
33 Work Function of Ru Oxide Metal Gate. *Electrochem. Solid-State Lett.* **2010**, *13* (4),  
34  
35 H105–H107.  
36  
37  
38 (42) Pantisano, L.; Schram, T.; Li, Z.; Lisoni, J. G.; Pourtois, G.; Gendt, S. De; Brunco, D. P.;  
39  
40 Akheyar, A.; Afanas, V. V; Shamuilia, S.; Stesmans, A.; Pantisano, L.; Schram, T.; Li, Z.;  
41  
42 Lisoni, J. G.; Pourtois, G.; Gendt, S. De. Ruthenium Gate Electrodes on SiO<sub>2</sub> and HfO<sub>2</sub> :  
43  
44 Sensitivity to Hydrogen and Oxygen Ambients. *Appl. Phys. Lett.* **2012**, *88*, 243514.  
45  
46  
47  
48 (43) Sun, Q.; Reuter, K.; Scheffler, M. Hydrogen Adsorption on RuO<sub>2</sub>(110): Density-  
49  
50 Functional Calculations. *Phys. Rev. B - Condens. Matter Mater. Phys.* **2004**, *70* (23), 1–  
51  
52 12.  
53  
54  
55  
56  
57  
58  
59  
60

- 1  
2  
3 (44) Sun, Q.; Reuter, K.; Scheffler, M. Effect of a Humid Environment on the Surface  
4 Structure of RuO<sub>2</sub> (100). *Phys. Rev. B* **2003**, *67* (20), 205424.  
5  
6  
7  
8  
9 (45) Ryden, W. D.; Lawson, A. W. Electrical Transport Properties of IrO<sub>2</sub> and RuO<sub>2</sub>. *Phys.*  
10 *Rev. B* **1970**, *1* (4), 1494–1500.  
11  
12  
13  
14 (46) Rothschild, J. A.; Eizenberg, M. Work Function Calculation of Solid Solution Alloys  
15 Using the Image Force Model. *Phys. Rev. B* **2010**, *81*, 224201–1 – 224201–224208.  
16  
17  
18  
19  
20 (47) Yun, J.; Park, M.; Rhee, S. Comparison of Tetrakis (dimethylamido) Titanium and  
21 Tetrakis (diethylamido) Titanium as Precursors for Metallorganic Chemical Vapor  
22 Deposition of Titanium Nitride. *J. Electrochem. Soc.* **1999**, *146* (5), 1804–1808.  
23  
24  
25  
26  
27  
28  
29  
30

## TOC GRAPHIC

